Laser directed energy deposition of FeSi/SS 316L advanced bimetallic high-speed rotors: From material characterization to performance evaluation

Original
Laser directed energy deposition of FeSi/SS 316L advanced bimetallic high-speed rotors: From material characterization to performance evaluation / Gianassi, C., Liverani, E., Cavagnino, A., Zarri, L., Ascari, A., Cui, Y., Fortunato, A.. - In: ADVANCES IN INDUSTRIAL AND MANUFACTURING ENGINEERING. - ISSN 2666-9129. - ELETTRONICO. - 11:(2025). [10.1016/j.aime.2025.100175]

Publisher:
Elsevier

Published
DOI:10.1016/j.aime.2025.100175

2025 IEEE Energy Conversion Congress and Exposition (ECCE) | 979-8-3315-4130-9/25/$31.00 ©2025 IEEE | DOI: 10.1109/ECCE58356.2025.11260106

100+ krpm Open-End Winding Reluctance Motor Drive With a Floating Capacitor Bridge

Deekshitha Srinivas Nayak
Dept. of Electrical, Electronic and Information Engineering "G. Marconi"
University of Bologna, Italy
Bologna, Italy
http://orcid.org/0000-0003-1054-8961

Gabriele Rizzoli
Dept. of Electrical, Electronic and Information Engineering "G. Marconi"
University of Bologna
Bologna, Italy
https://orcid.org/00000-0003-0119-3679

Michele Mengoni
Dept. of Electrical, Electronic and Information Engineering "G. Marconi"
University of Bologna
Bologna, Italy
https://orcid.org/0000-0002-6639-3017

Luca Zarri
Dept. of Electrical, Electronic and Information Engineering "G. Marconi"
University of Bologna
Bologna, Italy
https://orcid.org/0000-0002-5630-2126

Angelo Tani
Dept. of Electrical, Electronic and Information Engineering "G. Marconi"
University of Bologna
Bologna, Italy
https://orcid.org/0000-0003-2347-8480

Andrea Cavagnino
Dipartimento Energia "G. Ferraris"
Politecnico di Torino
Torino, Italy
https://orcid.org/0000-0003-0636-9012

***Abstract* — This paper presents the development of a high-speed electric drive based on a three-phase synchronous reluctance motor with a bimetallic rotor manufactured via additive manufacturing. The motor features an open-end stator winding and is supplied by a dual SiC-based inverter system consisting of two three-phase, three-level T-type inverters incorporating a floating capacitor. The floating capacitor topology enables the main inverter to operate at unity power factor. A coordinated control strategy manages both converters to maximize active power output while maintaining voltage and current within their limits and ensuring DC-link voltage balancing in the three-level converter. The paper describes the drive architecture, control scheme, and technical solutions adopted to achieve high-speed operation.**

Keywords—Open-End Windings, SyncRel motor drives, GaN-based power converters, Variable Speed Drive.

I. INTRODUCTION

Interior Permanent Magnet (IPM) synchronous machines are widely recognized as the most effective solution for high-speed applications, owing to their superior torque and power densities and broad constant-power speed range. However, increasing concern over the fluctuating cost and supply chain vulnerabilities associated with rare-earth permanent magnets—such as neodymium–iron–boron—has motivated the exploration of alternative electric drive technologies that do not rely on rare-earth materials.

Among these alternatives, Synchronous Reluctance (SyncRel) machines have emerged as a promising option. Although they exhibit lower torque and power densities compared to IPM machines, SyncRel motors demonstrate higher efficiencies than induction machines in high-speed operation. Furthermore, recent advancements in additive manufacturing have enabled the fabrication of quasi-solid rotors with enhanced anisotropy, making SyncRel machines increasingly viable for very high-speed, rare-earth-free applications [1].

To further improve the performance of synchronous machines in high-speed drives, various power converter topologies have been proposed. One particularly attractive approach involves the use of two inverters to supply an open-end winding machine. As shown in Fig. 1(a), the secondary inverter can be connected via a floating capacitor, which eliminates zero-sequence current circulation [2]–[3]. This dual-inverter topology improves the utilization of the primary DC

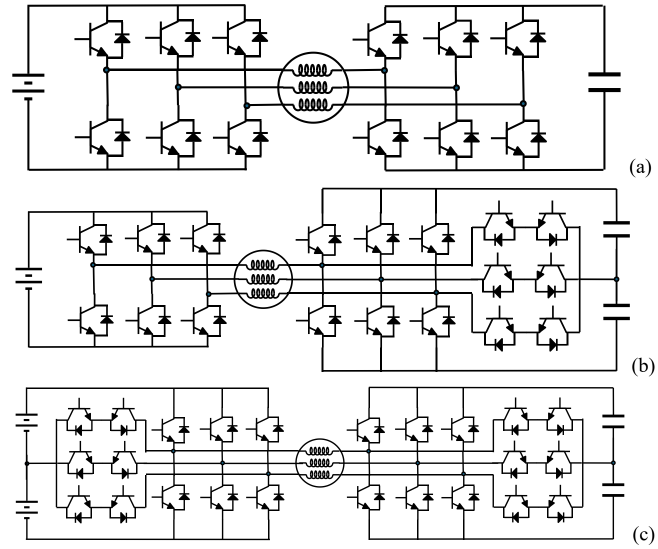

Fig. 1. Scheme of a dual inverter system with two two-level converters (a), a two-level inverter and a three-level floating capacitor T-type converter (b), or two T-type three-level converters (c).

Funded by the European Union - NextGenerationEU under the National Recovery and Resilience Plan (PNRR) - Mission 4 Education and research - Component 2 From research to business - Investment 1.1, Notice Prin 2022 - (DD N. 104 del 2/2/2022), title "TUrBO: the next 100,000+rpm synchronous reluctance motor drives", proposal code 202292E4FS - CUP J53D23000650006. This manuscript reflects only the authors' views and opinions, and the Ministry cannot be considered responsible for them.

979-8-3315-4130-9/25/$31.00 ©2025 IEEE

power source and allows the secondary inverter to provide reactive power compensation. Under suitable conditions, the system can synthesize multilevel PWM waveforms at the stator terminals, thereby reducing current ripple—a critical factor in SyncRel machines designed with a low number of stator turns for low-voltage, high-speed applications [4]–[5]. Control schemes for such dual-inverter drives have been previously explored, particularly in the context of surface-mounted permanent magnet machines [6].

Recent studies have also addressed modulation strategies for dual-inverter systems employing different semiconductor technologies [7], [8]. Configurations using silicon (Si) switches for the primary inverter and silicon carbide (SiC) switches for the secondary inverter have demonstrated that increasing the voltage level of the secondary inverter extends the drive's operational speed range [9]–[11]. Moreover, as shown in Figs. 1(b)-(c), the adoption of multilevel inverter topologies has been proposed as an alternative to conventional two-level converters to further enhance current waveform quality [12]-[13].

This work investigates a novel open-end winding SyncRel motor drive configuration consisting of two three-phase three-level inverters. The schematic of the proposed drive is shown in Fig. 1(c). The system is designed to achieve rotational speeds of 100 krpm while addressing the inherently low power factor of SyncRel machines—typically around 0.7 at base speed—through reactive power compensation provided by the floating capacitor converter. Consequently, the required DC voltage of the main inverter can be reduced by up to 30% compared to conventional single-inverter drives [14].

The objective of this study is the development of a robust field-oriented control system that maximizes the torque and power output of the motor within defined electrical constraints. The remainder of this paper is organized as follows: Section II presents the SyncRel motor model with open-end stator winding and discusses the voltage and current limitations governing its operation. Section III describes the proposed control strategy, and Section IV reports the experimental validation of the system.

II. MODEL OF THE ELECTRIC DRIVE

A. *Equations of the Machine and the Bridge with a Floating Capacitor*

The behavior of the SyncRel machine fed by a dual-inverter drive can be accurately represented in the well-known *d-q* reference frame, which is synchronous with the rotor. The *d*-axis is aligned with the direction of minimum inductance. Fig. 2 illustrates the configuration of the dual-inverter system under investigation.

The dynamic model of the SyncRel machine in the *d-q* frame is given by the following equations:

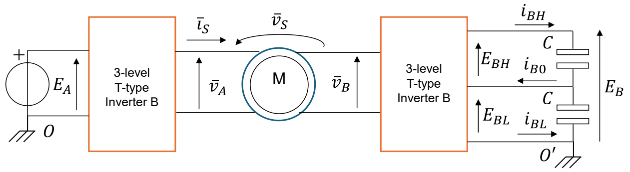

Fig. 2. Schematic of the SyncRel drive based on the space vector representation.

$$v_{Sd} = R_S i_{Sd} - \omega\varphi_{Sq} + \frac{d\varphi_{Sd}}{dt} \tag{1}$$

$$v_{Sq} = R_S i_{Sq} + \omega\varphi_{Sd} + \frac{d\varphi_{Sq}}{dt} \tag{2}$$

$$\varphi_{Sd} = L_{Sd} i_{Sd} \tag{3}$$

$$\varphi_{Sq} = L_{Sq} i_{Sq} \tag{4}$$

$$T = \frac{3}{2} p\left(L_{Sd} - L_{Sq}\right) i_{Sd} i_{Sq} \tag{5}$$

where p is the number of pole pairs, ω is the electric rotor speed, T is the electromagnetic torque, i_{Sd} and i_{Sq} are the $d-q$ components of the stator current vector $\bar{\imath}_S$, v_{Sd} and v_{Sq} are the $d-q$ components of the stator voltage vector $\bar{v}_S$, φ_{Sd} and φ_{Sq} are the $d-q$ components of the stator flux vector $\bar{\varphi}_S$, R_S is the stator resistance, and L_{Sd} and L_{Sq} are the stator inductances, with $L_{Sq} > L_{Sd}$.

The voltage space vector applied to the motor terminals results from the difference between the output voltages of the two inverters:

$$\bar{v}_S = \bar{v}_A - \bar{v}_B \tag{6}$$

where $\bar{v}_A$ and $\bar{v}_B$ are the voltage vectors generated by inverters A and B, respectively.

Assuming negligible inverter losses, the time derivative of the energy stored in the floating capacitors of inverter B equals the instantaneous power absorbed by that inverter.

$$\frac{1}{2} C \frac{d}{dt}\left(E_{BH}^2 + E_{BL}^2\right) = P_B \tag{7}$$

where E_{BH} and E_{BL} are the voltages across the high-side and low-side capacitors of the T-type inverter B, C is the capacitance value, and P_B is the instantaneous power absorbed by inverter B.

The voltage imbalance across the two capacitors can be regulated by controlling the current i_{B0} flowing through the midpoint of the capacitor leg:

$$C \frac{d}{dt}\left(E_{BH} - E_{BL}\right) = i_{B0}. \tag{8}$$

The sum of the capacitor voltages E_{BH} and E_{BL} is the total DC-link voltage E_B of the three-level converter B.

B. *Voltage and Current Constraints*

The stator current magnitude is constrained by the maximum allowable value I_{max} , representing either the rated thermal current under steady-state operation or the maximum permissible value under overload conditions. Moreover, the voltage magnitudes generated by inverters A and B must not exceed their respective limits $V_{A,max}$ and $V_{B,max}$, determined by the available DC-link voltages and the employed modulation techniques:

$$|\bar{v}_A| \leq V_{A,max} \tag{9}$$

$$|\bar{v}_B| \leq V_{B,max} \tag{10}$$

For modulation strategies such as space vector modulation or PWM with third-harmonic injection, the voltage limits are defined as follows:

$$V_{A,max} = \frac{E_A}{\sqrt{3}} \tag{11}$$

$$V_{B,max} = \frac{E_B}{\sqrt{3}} \tag{12}$$

where E_A is the DC-link voltage of inverter A.

C. Energy Control of the Floating Capacitor Bridge

The output voltage $\bar{v}_B$ of the floating capacitor bridge can be decomposed into components parallel and orthogonal to the stator current vector:

$$\bar{v}_B = \left(v_B^P + j v_B^Q\right)\frac{\bar{\imath}_S}{|\bar{\imath}_S|}. \tag{13}$$

In (13), v_B^P determines the active power exchanged by inverter B, while v_B^Q determines the reactive power. Accordingly, the instantaneous active and reactive powers are given by the following expressions:

$$P_B = \frac{3}{2} Re\{\bar{\imath}_S \bar{v}_B^*\} = \frac{3}{2} v_B^P |\bar{\imath}_S| \tag{14}$$

$$Q_B = \frac{3}{2} Im\{j\bar{\imath}_S \bar{v}_B^*\} = \frac{3}{2} v_B^Q |\bar{\imath}_S| \tag{15}$$

where "*" is complex conjugate operator.

Substituting (14) into (7) yields:

$$\frac{1}{2} C \frac{d}{dt}\left(E_{BH}^2 + E_{BL}^2\right) = \frac{3}{2} v_B^P |\bar{\imath}_S|. \tag{16}$$

Equation (16) shows that the energy stored in the floating capacitors depends solely on the parallel component $\bar{v}_B$. In steady-state conditions, maintaining energy balance requires $v_B^P = 0$.

The orthogonal component v_B^Q is used to control the reactive power delivered by inverter B. The total reactive power supplied by inverter A, Q_A, can be expressed as

$$Q_A = \frac{3}{2} \bar{v}_A \cdot j\bar{\imath}_S = Q_S + Q_B. \tag{17}$$

where Q_S is the reactive power of the SyncRel machine.

Regulating Q_B to ensure $Q_A = 0$ allows inverter A to operate at unity power factor, thus maximizing the active power transfer under current and voltage constraints. Assuming negligible stator resistances and applying steady-state conditions to (1) and (2), (17) becomes:

$$Q_A \cong \frac{3}{2}(j\omega\bar{\varphi}_S) \cdot j\bar{\imath}_S + \frac{3}{2}\bar{v}_B \cdot j\bar{\imath}_S \tag{18}$$

Using (13) and setting (18) to zero, the value for v_B^Q is obtained:

$$v_B^Q = -\frac{\omega\bar{\varphi}_S \cdot \bar{\imath}_S}{|\bar{\imath}_S|}. \tag{19}$$

However, this value may exceed the maximum allowed voltage defined by (10), especially at high speeds. In such cases, the orthogonal component is saturated, leading to the following steady-state expression for $\bar{v}_B$:

$$\bar{v}_B = -j(sgn\,\omega)\ V_{B,max}\frac{\bar{\imath}_S}{|\bar{\imath}_S|}. \tag{20}$$

Equations (6)-(20) form the basis for the control scheme implemented in the proposed dual-inverter SyncRel drive.

D. Control of the Floating-Capacitor Unbalance

For proper operation of the three-level T-type inverter, the voltages across the high-side and low-side capacitors, E_{BH} and E_{BL}, must be maintained close to the reference value $E_{B,ref}/2$. As indicated in (8), any voltage imbalance can be corrected by controlling the current i_{B0}, which flows through the midpoint of the capacitor leg.

It is established that the average value of i_{B0} over a switching period is determined by the common-mode voltage v_{B0} of inverter B. The modulation strategy links this common-mode voltage to the leg modulation signals m_{Bk} (for $k = 1,2,3$) through the relationship:

$$m_{Bk} = m_{B0} + n_{Bk} \quad k = 1, 2, 3 \tag{21}$$

where m_{B0} is the zero-sequence modulation component, defined as

$$m_{B0} = \frac{v_{B0}}{E_B} \tag{22}$$

and n_{Bk} is the normalized reference voltage for the *k*th phase leg, given by

$$n_k = \frac{v_{Bk}}{E_B} \qquad (k = 1, 2, 3). \tag{23}$$

To remain within the linear modulation region, the leg modulation signals m_{Bk} must satisfy the condition $0 \leq m_{Bk} \leq 1$. This constraint imposes the following bounds on the zero-sequence component m_{B0}:

$$m_{B0,min} \leq m_{B0} \leq m_{B0,max} \tag{24}$$

where:

$$\begin{aligned} m_{B0,min} &= -\min_{k=1,2,3}\{n_{Bk}\} \\ m_{B0,max} &= 1 - \max_{k=1,2,3}\{n_{Bk}\}. \end{aligned} \tag{25}$$

Assuming single-step modulation, the midpoint current i_{B0} can be expressed as a linear combination of the phase currents i_{Sk} ($k = 1,2,3$) as follows:

$$i_{B0} = -\sum_{k=1}^{3} m_{Mk} i_{Sk}. \tag{26}$$

The weighting factor m_{Mk} depend on the modulating signal m_{Bk} and the threshold parameter λ, which represents the ratio between the lower capacitor voltage E_{BL} and the total DC-link voltage E_B:

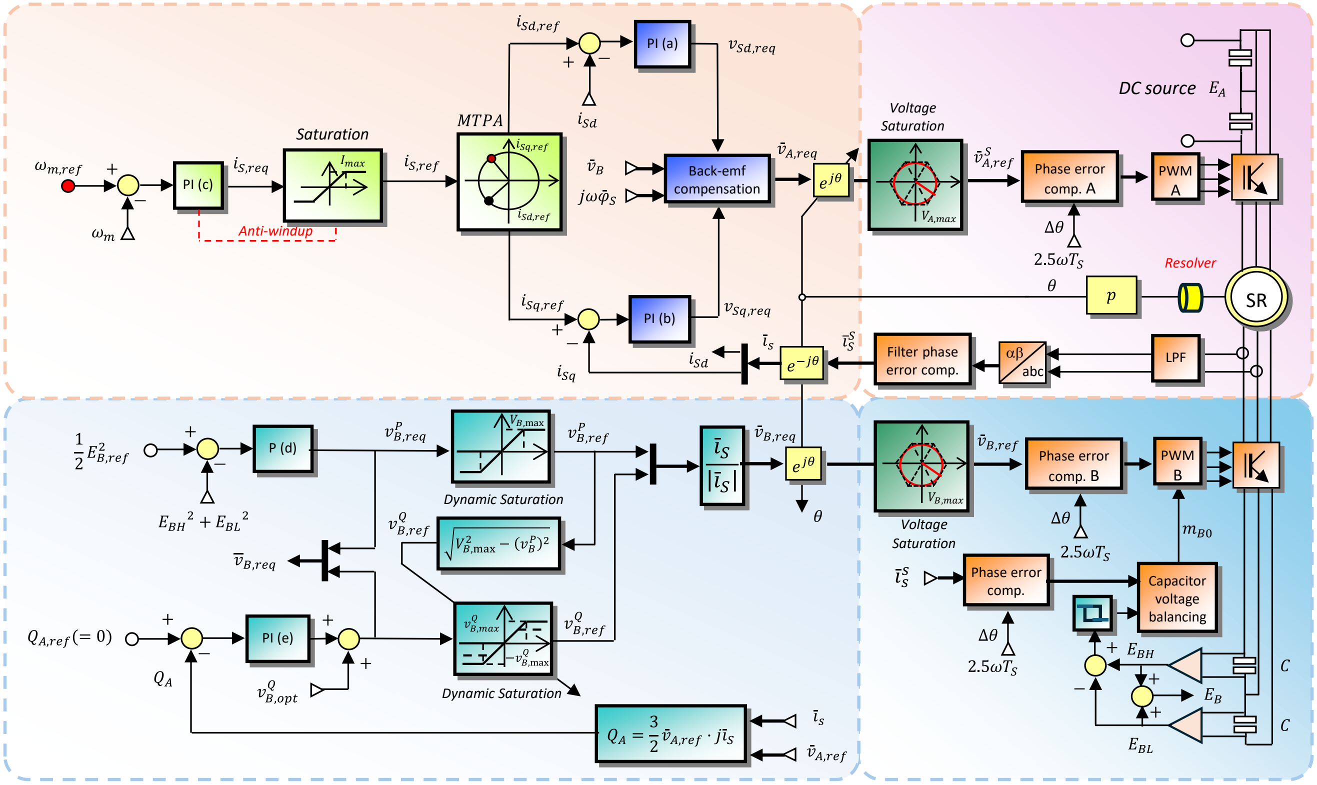

Fig. 3. Control scheme of the SyncRel motor drive with an open-end stator winding.

$$m_{Mk} = \begin{cases} \dfrac{1-m_{Bk}}{1-\lambda} & if\ m_{Bk} \geq \lambda \\ \dfrac{m_{Bk}}{\lambda} & if\ m_{Bk} < \lambda \end{cases}. \tag{27}$$

The zero-sequence component m_{B0} can thus be used not only to balance the capacitor voltages but also to reduce switching losses. For example, setting $m_{B0} = m_{B0,min}$ results in one of the lower switches of the T-type inverter remaining fully on for the entire switching period, causing the corresponding phase leg to avoid commutation. The resulting midpoint current under this condition is denoted $i_{B0,min}$.

Similarly, when $m_{B0} = m_{B0,max}$, the upper switch of an inverter leg remains active for the full switching period, producing a midpoint current referred to as $i_{B0,max}$.

The values of $i_{B0,min}$ and $i_{B0,max}$ can be computed by applying (21), (26), and (27). Under steady-state operating conditions, these two current values can exhibit opposite signs in a switching period. Consequently, the control system can dynamically select between $m_{B0,min}$ or $m_{B0,max}$, thereby imposing two distinct slopes for the time derivative (8) during each switching cycle. However, when the three-level inverter primarily exchanges reactive power and just a small amount of active power, the signs of $i_{B0,min}$ and $i_{B0,max}$ may be equal. Luckily, these signs fluctuate between +1 to -1 over one electrical fundamental period. In this case, the adopted strategy selects the value of m_{B0} that leads to the lowest imbalance, and the system remains stable over the fundamental period. This strategy enables active control of the floating capacitor balance while reducing commutations and associated switching losses.

III. CONTROL SCHEME

Fig. 3 illustrates the control architecture of the dual-inverter system, organized into functional blocks. The first block governs inverter A, which is directly connected to the main power source and implements the control of speed and stator currents. The second block is dedicated to reactive power compensation and regulation of the DC-link voltage of multilevel inverter B. The third and fourth blocks describe the modulation strategies applied to Inverters A and B, respectively.

A. *Control of Speed and Stator Currents*

The overall control scheme is based on field-oriented control implemented in the rotor-synchronous $d-q$ reference frame [15]. The stator current components i_{Sd} and i_{Sq} are regulated by PI controllers (a) and (b), respectively. Feed-forward terms are added to the controller outputs to compensate both the back electromotive force (EMF) of the motor, $j\omega\bar{\varphi}_S$, and the voltage contribution from inverter B.

The references for the currents i_{Sd} and i_{Sq} are according to the maximum torque per ampere (MTPA) strategy depending on the current request generated by PI controller (c), which processes the rotor speed error.

B. *Control of the Floating Capacitor and the Reactive Power*

The DC-link voltage of inverter B, E_B, is regulated by PI controller (d), which adjusts the voltage component v_B^P in accordance with (16). Concurrently, PI regulator (e) enforces a unity power factor at the terminals of inverter A by driving its reactive power Q_A to zero. To enhance the dynamic performance, the output of regulator (e) is augmented with a feedforward term based on the orthogonal voltage component, v_B^Q, computed as in (19)-(20).

To maintain capacitor voltage balance, a hysteresis controller monitors the voltage differential $E_{BH} - E_{BL}$ and selects the sign of the midpoint current i_{B0} accordingly. The zero-sequence modulation componentm_{B0} is then set to either $m_{B0,max}$ or $m_{B0,min}$, based on which value produces a corrective current ($i_{B0,max}$ or $i_{B0,min}$) that better compensates the imbalance, as derived in (21), (26), and (27). Although the balancing action may not be effective within a single switching cycle, it has been verified to converge effectively over an electrical fundamental period, maintaining capacitor voltage symmetry and stable multilevel operation.

C. Correction of the Phase Errors at High Speed

At high rotor speeds, the ratio between switching frequency and fundamental frequency—referred to as the frequency modulation index—decreases. This leads to systematic errors in the inverter output voltage due to pulse-width modulation (PWM) and digital control delays. Assuming a reference voltage of the form $\bar{V}_{ref} e^{j2\pi f t}$, the average output voltage over a switching period T_S can be approximated as follows:

$$\begin{aligned} \bar{v}_{PWM}(t) &= \frac{1}{T_S}\int_{t-T_S}^{t} \bar{V}_{ref} e^{j\omega t} dt \\ &= \bar{V}_{ref} e^{j\omega\left(t-\frac{T_S}{2}\right)} \mathrm{sinc}\left(\frac{\omega T_S}{2\pi}\right) \end{aligned} \tag{28}$$

where $\mathrm{sinc}(x) = \frac{\sin(\pi x)}{\pi x}$. Considering the additional delay introduced by digital control computation—typically one or two full switching periods—the effective mean output voltage becomes:

$$\bar{v}_{PWM}(t) = \bar{V}_{ref} e^{j\omega(t-2.5T_S)} \mathrm{sinc}\left(\frac{\omega T_S}{2\pi}\right). \tag{29}$$

To compensate for this phase and magnitude error, the reference voltage $\bar{V}_{ref}$ must be pre-rotated by a phase advance of $2.5\omega T_S$ and scaled by $1/\mathrm{sinc}\left(\frac{\omega T_S}{2\pi}\right)$. However, since $\mathrm{sinc}(\frac{\omega T_S}{2\pi}) \cong 1$ in typical operating conditions, the scaling factor is often negligible, and only the phase correction is applied.

In addition to the phase lag introduced by the digital control and modulation process, the delay caused by the second-order input low-pass filter used for current measurement must also be considered. This filter is typically employed to attenuate switching harmonics and noise in the acquired stator current signals. As a result, the measured stator current vector is affected by a frequency-dependent phase lag and must be compensated by applying a corrective rotation $e^{j\theta_f(\omega)}$, where $\theta_f(\omega)$ denotes phase shift introduced by the filter at the angular frequency ω.

Furthermore, to predict the actual current values corresponding to the forthcoming switching configuration of inverter B—used for capacitor voltage balancing—the compensated stator current vector is further rotated by $e^{j2.5\omega T_S}$. This additional term accounts for the control computation delay. The resulting stator current vector is then used in (26) to compute the midpoint current i_{B0} required for effective balancing of the floating capacitor voltages.

IV. EXPERIMENTAL RESULTS

An experimental validation was carried out to assess the effectiveness of the proposed control strategy. The test setup is based on a two-pole synchronous reluctance machine developed within the framework of the Italian national research project TUrBO 2022 [16]. The motor features an Axially-Laminated Anisotropic (ALA) rotor design and is intended for additive manufacturing. The rotor structure consists of alternating layers of 316L stainless steel and FeSi 2.9%, with variable layer thicknesses to enhance anisotropy and mechanical integrity at high rotational speeds. Fig. 4 shows the prototype, which consists of a single housing that integrates the SyncRel motor developed in the TUrBO project and a surface permanent magnet machine used as the mechanical load. The system is equipped with water cooling for thermal management, and a resolver is mounted on the SyncRel motor side for rotor position feedback.

The key parameters of the prototype motor are summarized in Table I. The machine rated power is 1 kW, which is achieved at approximately 100,000 rpm. Although the nominal phase voltage is 185 $\mathrm{V_{rms}}$, the stator insulation system is designed to withstand significantly higher voltages, allowing flexibility in converter selection and modulation techniques.

In the experimental setup, the DC-link voltage of inverter B was selected to be at least 20% higher than that of inverter A, in accordance with design considerations and previous studies [14].

Both inverters are implemented using SiC power devices and operate at a switching frequency of 30 kHz, ensuring high efficiency and reduced current ripple. The inverter deadtimes are 400 ns. The effectiveness of the control strategy — including power factor compensation, and floating capacitor voltage balancing—was verified experimentally and is discussed in the following subsections.

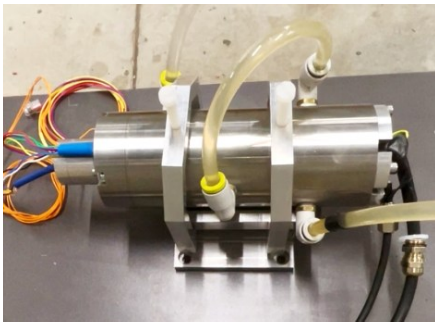

Fig. 4. Photograph of the experimental setup.

TABLE I – MACHINE PARAMETERS

$P_{m,max}$	=	1	kW	L_d	=	2.5	mH
$I_{S,rated}$	=	3.4	A_{rms}	L_q	=	8.6	mH
$V_{S,rated}$	=	185	V_{rms}	J_m	=	$4.5 \cdot 10^{-6}$	Kg m^2
ω_{rated}	=	100	krpm (@$P_{m,max}$)	J_{load}	=	$1 \cdot 10^{-5}$	Kg m^2
p	=	1		$\cos\varphi$	=	0.606	
C	=	200	μF				
R_S	=	1.764	Ω (@ 90°C)				

A. Steady-State Performance

Fig. 5 shows the steady-state behavior of the motor operating at 100 krpm operating at no load. The DC-link voltages of inverter A and inverter B are set to 170 V and 200 V, respectively. The top waveform shows the motor phase current, which is nearly sinusoidal with negligible ripple, confirming the effectiveness of the multilevel modulation and current control. The subsequent plots display the pole voltages of the first leg of inverters A and B. The pole voltage of inverter A is observed to be in phase with the corresponding phase current, indicating active power delivery, whereas the pole voltage of inverter B is approximately in quadrature, consistent with its role in reactive power compensation. The bottom plot illustrates the resulting phase voltage and its low-pass filtered version. The phase voltage clearly exhibits a multilevel structure, demonstrating the combined effect of both inverters in generating high-quality voltage waveforms.

Fig. 6 shows the behavior of the drive operating at 40 krpm. The waveforms are analogous to those in Fig. 5, including the phase current and the pole voltages of the first leg of inverters A and B. The bottom trace shows the DC-link voltage of inverter B in place of the phase voltage. The DC-link voltage remains stable, with negligible oscillation, confirming the effectiveness of the capacitor voltage balancing strategy.

B. Transient Performance

Fig. 7 displays, from top to bottom, the phase current, the pole voltage of inverter A (first leg), the rotor speed and the DC-link voltage of inverter B. The DC-link voltage is pre-charged before motor start-up, as evident from the initial condition. During the acceleration phase, the phase current increases to provide the required electromagnetic torque and subsequently decreases as the motor reaches steady-state. At steady-state, the current stabilizes at a low value, compensating for frictional losses. The pole voltage of inverter A varies throughout the transient, adapting to the evolving operating conditions. The DC-link voltage of inverter B remains stable during the entire transient, demonstrating effective voltage regulation and energy management.

Fig. 8 shows the dynamic response of the system as the power-factor correction algorithm is enabled. Initially, the power factor is approximately 0.5, indicating a significant reactive power component. Upon activation of the power factor correction algorithm, the power factor progressively increases and reaches unity. This transition is reflected in the behavior of the pole voltage, which gradually shifts to become in phase with the stator current of inverter A, confirming successful compensation of reactive power. Two detailed views are provided, highlighting the motor operation before and after enabling the correction algorithm.

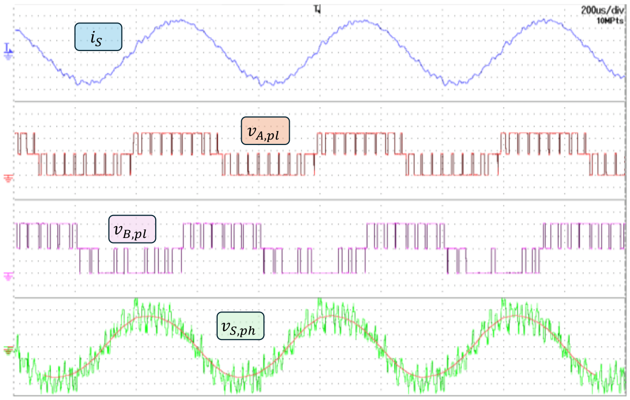

Fig. 5. Steady-state operation of the TUrBO motor at 100,000 rpm at no load. From top to bottom: phase current (1 A/div), pole voltage of inverter A (50 V/div), pole voltage of inverter B (50 V/div), phase voltage (50 V/div).

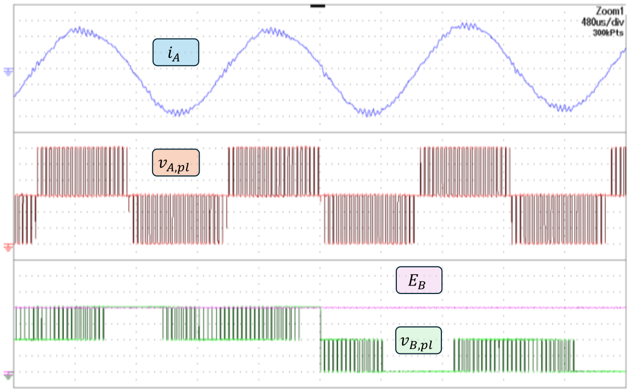

Fig. 6. Steady-state operation of the TUrBO motor at 40,000 rpm. From top to bottom: phase current (2 A/div), pole voltage of inverter A (25 V/div), pole voltage of inverter B (50 V/div), DC-link voltage of inverter B (50 V/div).

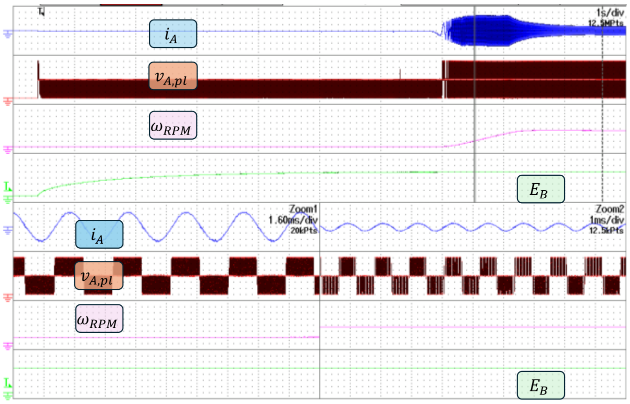

Fig. 7. Start-up transient of the TUrBO motor up to 50 krpm. From top to bottom: phase current (2 A/div), pole voltage of inverter A (25 V/div), motor speed (20 krpm/div), DC-link voltage of inverter B (50 V/div).

Fig. 9 illustrates the behavior of the motor when the load torque increases linearly from zero to its rated value over a 1-second interval. The DC-link voltages of Inverters A and B are set to 200 V and 250 V, respectively. Throughout the transient, the control system maintains stable operation. The rotor speed exhibits a slight reduction of approximately 4% during the torque increase; however, this variation is too small to be clearly discernible in the figure. The system effectively

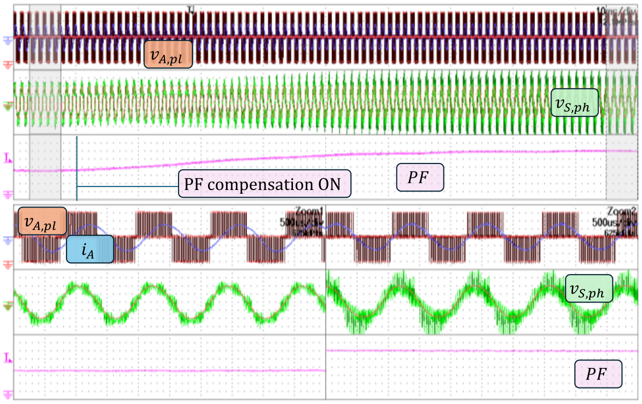

Fig. 8. Performance of the power-factor compensation when the drive operates at 50 krpm. From top to bottom: phase current (1 A/div) and pole voltage of inverter A (25 V/div), actual and filtered waveform of the stator phase voltage (25 V/div), input power factor (0.2 pu/div).

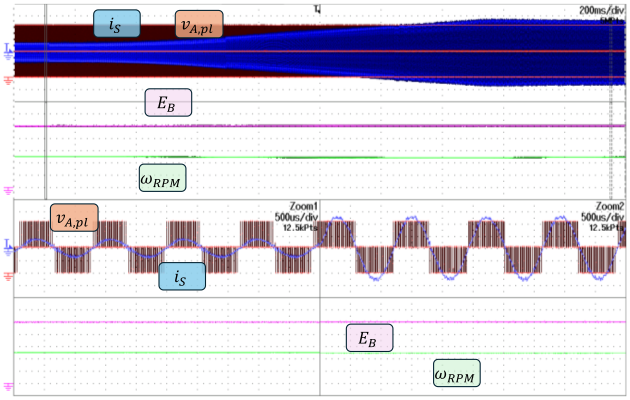

Fig. 9. Dynamic response of the drive system at 50 krpm under a torque ramp from 0 Nm to the rated torque. From top to bottom: phase current (2 A/div), pole voltage of inverter A (50 V/div), DC-link voltage of inverter B (50 V/div), rotor speed (20 krpm/div).

compensates for the increased load without compromising performance or waveform quality.

V. CONCLUSIONS

A dual-inverter control system for a SyncRel motor with open-end stator windings has been designed and experimentally validated. The proposed architecture consists of two three-level T-type inverters: the primary inverter is supplied by the main DC voltage source, while the secondary inverter incorporates a floating DC-link capacitor. This floating-capacitor bridge fulfills two key functions—providing reactive power compensation for the primary inverter and enabling voltage boosting to raise the motor terminal voltage.

Depending on the motor characteristics, the drive architecture offers several advantages. Operating the main inverter at unity power factor allows for a reduction in the required input DC-link voltage— up to 40% in rated conditions —while maintaining the same torque capability.

Experimental results confirm the effectiveness of the proposed solution and validate its feasibility for high-speed operation, demonstrating satisfactory power quality, efficient reactive power management, and acceptable performance under dynamic load conditions.

REFERENCES

[1] D. Newman et al., “Solid high-speed synchronous reluctance rotor enabled by multi-material additive manufacturing,” IEEE ECCE’23, Nashville, TN, USA, pp. 3965-3972, 2023.

[2] J. S. Park, K. Nam, “Dual inverter strategy for high operation of HEV permanent magnet synchronous motor,” in Industry Applications Conference, Tampa, FL, USA, 2006.

[3] T. Gerrits, C. G. E. Wijnands, J. J. H. Paulides, J. L. Duarte, “Dual voltage source inverter topology extending machine operating range,” ECCE 2012, Raleigh, NC, USA, 2012.

[4] Y. Lee, J.-I. Ha, “Power enhancement of dual inverter for open-end permanent magnet synchronous motor,” Applied Power Electronics Conference and Exposition (APEC), Long Beach, CA, USA, 2013.

[5] R. U. Haque, M. S. Toulabi, A. M. Knight, J. Salmon, “Wide speed range operation of PMSM using an open winding and a dual inverter drive with a floating bridge,” ECCE 2013, Denver, CO, USA, 2013.

[6] Shajjad Chowdhury, Patrick Wheeler, Chris Gerada, Saul Lopez Arevalo, “A dual inverter for an open-end winding induction motor drive without an isolation transformer,” APEC 2015, 15-19 March 2015, Charlotte, NC, USA, pp. 283- 289.

[7] L. Rovere, A. Formentini, G. Lo Calzo, P. Zanchetta, T. Cox, “IGBT-SiC dual fed open-end winding PMSM drive,” IEMDC 2017, 21-24 May 2017, Miami, USA, pp. 1-7.

[8] M. Pulvirenti, G. Scarcella, G. Scelba, A. Testa, “On-line stator resistance and permanent magnet flux linkage identification on open-end winding PMSM drives,” ECCE 2017, 1-5 Oct. 2017, Cincinnati, OH, USA, pp. 5869- 5876.

[9] C. Perera, S. Leng, G. J. Kish and J. Salmon, "Robust floating capacitor voltage control of dual inverter drive for open-ended winding induction motor," 2019 IEEE APEC, Anaheim, CA, USA, 2019, pp. 249-256.

[10] S. Wdaan, C. Perera and J. Salmon, "Field weakening operation of open-winding induction motor dual drives using a floating capacitor bridge inverter," 2021 ECCE, Vancouver, BC, Canada, 2021, pp. 4915-4920.

[11] A. Mizukoshi, H. Haga, and E. Sakasegawa, "Evaluation of the output voltage harmonics of typical PWM methods in a dual-inverter fed open-end winding induction motor with a floating-capacitor," 2021 IEEE ECCE, Vancouver, BC, Canada, 2021, pp. 4896-4901.

[12] M. G. Majumder, A. K. Yadav, K. Gopakumar, K. Raj R, U. Loganathan, and L. G. Franquelo, "A 5-level inverter scheme using single dc link with reduced number of floating capacitors and switches for open-end IM drives," in IEEE Trans. on Ind. Electronics, vol. 67, no. 2, pp. 960-968, Feb. 2020.

[13] A. Amerise, L. Rovere, A. Formentini, M. Mengoni, L. Zarri, and P. Zanchetta, "Electric drive based on an open-end winding surface PM synchronous machine with a floating capacitor bridge," IEEE Trans. on Ind. Appl., vol. 56, no. 3, pp. 2709-2718, May-June 2020.

[14] Z. Huang, T. Yang, P. Giangrande, S. Chowdhury, M. Galea, and P. Wheeler, “Enhanced performance of dual inverter with a floating capacitor for motor drive applications,” *IEEE Trans. Power Electron.*, vol. 36, no. 6, pp. 6903-6916, June 2021.

[15] R. Testa et al., "Open-end winding SyncRel motor drive with a floating capacitor bridge for high-speed applications," 2024 IEEE Energy Conversion Congress and Exposition (ECCE), Phoenix, AZ, USA, 2024, pp. 6163-6169.

[16] Y. Cui, C. Gianassi, A. Fortunato, L. Zarri and A. Cavagnino, "High-Speed Synchronous Reluctance Motors with Additively Manufactured Rotors," 2024 IEEE Energy Conversion Congress and Exposition (ECCE), Phoenix, AZ, USA, 2024, pp. 5024-5031, October 2024.